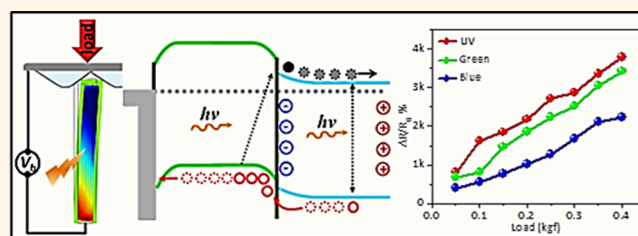


Piezo-phototronic Effect Enhanced UV/Visible Photodetector Based on Fully Wide Band Gap Type-II ZnO/ZnS Core/Shell Nanowire Array

Satish C. Rai,[†] Kai Wang,[†] Yong Ding,[‡] Jason K. Marmon,[¶] Manish Bhatt,[†] Yong Zhang,[¥] Weilie Zhou,^{*,†} and Zhong Lin Wang^{*,‡,§}

[†]Advanced Materials Research Institute, University of New Orleans, New Orleans, Louisiana 70148, United States, [‡]School of Materials Science and Engineering, Georgia Institute of Technology, Atlanta, Georgia 30332-0245, United States, [¶]Nanoscale Science, University of North Carolina, Charlotte, North Carolina 28223, United States, [¥]Department of Electrical and Computer Engineering/Optoelectronic Center, University of North Carolina, Charlotte, North Carolina 28223, United States, and [§]Beijing Institute of Nanoenergy and Nanosystems, Chinese Academy of Sciences, 100083 Beijing, China

ABSTRACT A high-performance broad band UV/visible photodetector has been successfully fabricated on a fully wide bandgap ZnO/ZnS type-II heterojunction core/shell nanowire array. The device can detect photons with energies significantly smaller (2.2 eV) than the band gap of ZnO (3.2 eV) and ZnS (3.7 eV), which is mainly attributed to spatially indirect type-II transition facilitated by the abrupt interface between the ZnO core and ZnS shell. The performance of the device was further enhanced through the piezo-phototronic effect induced lowering of the barrier height to allow charge carrier transport across the ZnO/ZnS interface, resulting in three orders of relative responsivity change measured at three different excitation wavelengths (385, 465, and 520 nm). This work demonstrates a prototype UV/visible photodetector based on the truly wide band gap semiconducting 3D core/shell nanowire array with enhanced performance through the piezo-phototronic effect.



KEYWORDS: UV/visible photodetector · piezo-phototronic effect · core/shell nanowire · type-II heterojunction

The piezo-phototronic effect has been applied to boost the optoelectronic performance of devices through coupling of semiconducting, optical, and piezoelectric properties in the ability to tune and control charge carrier generation, separation, transport, and/or recombination at an interface/junction.^{1,2} The inner piezopotential, generated due to strain in a non-centrosymmetric wurtzite semiconducting crystal, is the underlying mechanism provided that the materials selection and device design can enable the coupling in a favorable manner.³ This concept was first demonstrated in a single ZnO micro/nanowire based ultraviolet (UV) photodetector⁴ to increase the responsivity of the device by more than 500% under nominal (−0.36%) axial compressive strain. In spite of its excellent semiconducting and piezoelectric properties, application of ZnO as a photodetector is limited only to the UV region due

to its wide band gap ($E_g \sim 3.2$ eV). To overcome this limitation, a core/shell system, such as a single ZnO/CdS core/shell micro/nanowire,⁵ was utilized where sufficient photoabsorption could take place in the narrow band gap CdS shell layer. The strategy of using core/shell architecture not only allows the efficient use of intrinsic material properties from individual components but also improves the charge carrier collection favored by radial geometry where electrons and holes are spatially confined in different conducting channels of type-II heterostructures, which leads to reduced recombination losses.^{6–10} These core/shell nanowire features were further proven advantageous in a UV/visible photodetector integrated on a lateral structure composed of a carbon fiber/ZnO/CdS double shell microwire¹¹ and, more recently, in an optical-fiber-nanowire hybrid structure.¹² The promising attributes of core/shell nanowires

* Address correspondence to wzhou@uno.edu (W.Z.), zhong.wang@mse.gatech.edu (Z.L.W.).

Received for review April 7, 2015 and accepted June 3, 2015.

Published online June 03, 2015
10.1021/acsnano.5b02081

© 2015 American Chemical Society

could be further augmented in three-dimensional arrays where photoabsorption was enhanced by the trapping and rescattering of incident photons.¹³ Additionally, in nanowire arrays, simultaneous multi-channel charge transport facilitates efficient collection of photo generated electron–hole pairs, thereby leading to improved quantum efficiency,^{14,15} which when combined with the piezo-phototronic effect, opens up a new avenue for achieving significantly enhanced device performance.¹⁶ Moreover, the type-II heterostructure may extend the photoresponse spectral range to a significantly longer wavelength that is determined by the lower bandgap component.^{8,10,17} Herein, we report an efficient and highly sensitive broad band UV/visible photodetector based on fully wide band gap, three-dimensional (3D) ZnO/ZnS core/shell nanowire array in which the type-II transition plays a crucial role. More importantly, the device efficiency can be further improved, at least, by an order of magnitude rendering three orders of increase in relative responsivity by piezo-phototronic effect.¹⁸

RESULTS AND DISCUSSION

Figure 1 represents the structural characterization of a ZnO/ZnS core/shell nanowire array, where Figure 1a, b are top views of low magnification field emission scanning electron microscope (FESEM) images of the as-grown ZnO nanowire array and a ZnO/ZnS core/shell nanowire on indium tin oxide coated (ITO) glass substrate.⁹ Rational density and smooth surface ZnO nanowires, with lengths and diameters in the range of 5–6 μm and 150–200 nm, respectively, can be seen in Figure 1a, whereas a slightly rough surface and

increased diameter, with few ZnS particulates deposited on the tips, is observed in Figure 1b for the core/shell nanowires.

A high resolution transmission electron microscope (HRTEM) image of a typical single ZnO/ZnS core/shell nanowire is displayed in Figure 1c, where two different lattice fringes corresponding to the zinc-blend ZnS shell and wurtzite ZnO core separated by an abrupt interface can be seen, which is similar to the previously reported work.¹⁹ Furthermore, Figure 1d illustrates an energy dispersive (EDS) line scan collected along the lateral direction of a core/shell nanowire, which shows the characteristic core/shell elemental distribution, further confirming the successful synthesis of ZnO/ZnS core/shell nanowires.^{20,21}

A 3D photodetector was integrated on ZnO/ZnS core/shell nanowire array by positioning the Ag/polyester zigzag electrode on top of the nanowire array for the contact formation at the nanowire tips only and to ensure optimal compression under applied load (inset in Figure 2d).²² Complete fabrication and device integration details can be found in the Experimental Section.

A typical I – V measurement of the photodetector integrated on 3D ZnO/ZnS core/shell nanowire array under a UV (385 nm) excitation source is displayed in Figure 3. It can be seen that the photocurrent increases with an increase in the UV illumination density resulting from the higher intensity influenced increment in the generation rate (G) of electron–hole pairs, within the limit of $h\nu > E_g$ and defined by $G = \alpha F(1 - R)e^{-\alpha x}$ where, α is the absorption coefficient, R is the surface reflectivity, and F is the incident photon flux.²³

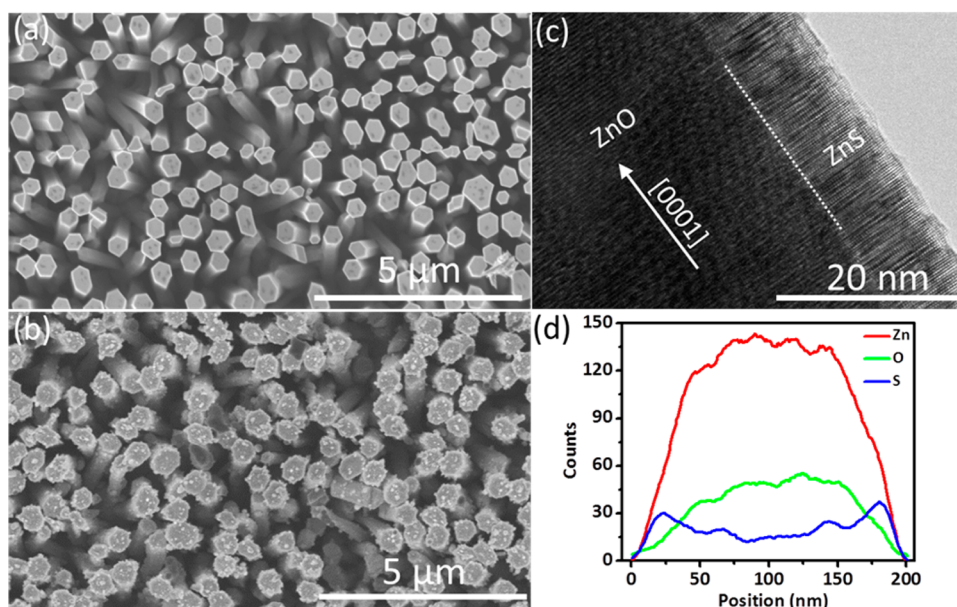


Figure 1. Structural characterization of a ZnO/ZnS core/shell nanowire showing low magnification top view, FESEM images of (a) an as-grown, ZnO nanowire array and (b) a ZnO/ZnS core/shell nanowire array, (c) an HRTEM image of a single ZnO/ZnS core/shell nanowire, and (d) the corresponding energy dispersive spectroscopy (EDS) lateral line scan depicting elemental peaks characteristic to core/shell nanowire structure.

Under steady state illumination at a fixed wavelength, the generation rate is solely determined by incident photon flux density (F), where an increase in F will improve the electron–hole pair generation rate. Because $E_{g,ZnS}$ (3.7 eV) $>$ E_{385nm} (3.22 eV) \approx $E_{g,ZnO}$ (3.2 eV), the excitation wavelength used only matches ZnO optical band gap, and it is reasonable to assume that the photocurrent contribution from the electron–hole

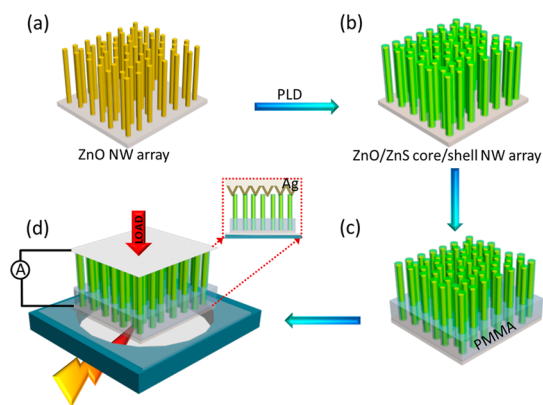


Figure 2. Schematic illustration of the ZnO/ZnS core/shell nanowire photodetector fabrication process. (a) ZnO nanowire array on ITO substrate synthesized through chemical vapor deposition (CVD), (b) a ZnS shell layer was deposited by pulsed laser ablation, (c) a $\sim 2 \mu\text{m}$ PMMA layer was spin coated onto the ZnO/ZnS core/shell nanowire array, and (d) the finished device mounted on a measurement cell. To achieve nanowire compression, load is applied on top of silver coated polyester zigzag electrode (inset of part d).

pairs predominantly arise from photoabsorption taking place in the ZnO core in a core/shell nanowire. In addition to band-to-band absorption in ZnO, the contribution from simultaneous indirect type-II transitions occurring between the valence band maxima of the ZnS_{VBM} to the conduction band minima of the ZnO_{CBM} has to be considered, and its effect on device performance will be discussed in details to follow. Variation in photocurrent with illumination intensity is plotted in Figure 3b, where an increase of 325% in photocurrent ($\sim 51 \mu\text{A}$) at an intensity of $1.32 \text{ mW}/\text{cm}^2$ can be seen as compared to the ($\sim 12 \mu\text{A}$) dark current. Time-dependent photocurrent measurement at a power density of $1.32 \text{ mW}/\text{cm}^2$ and bias of 1.5 V is shown in Figure 3c, which suggests stable device switching behavior. The performance of a practical photodetector is also characterized by its responsivity (R_λ) at a particular wavelength, which is an important parameter that is defined as¹⁶

$$R_\lambda = \frac{I_{\text{light}} - I_{\text{dark}}}{P_{\text{ill}}}$$

$$P_{\text{ill}} = I_{\text{ill}} \cdot A$$

where I_{light} and I_{dark} are currents when the photodetector is under illumination and in the dark, respectively. P_{ill} , I_{ill} , and A are the excitation power, illumination density, and the active/illuminated device area, respectively.

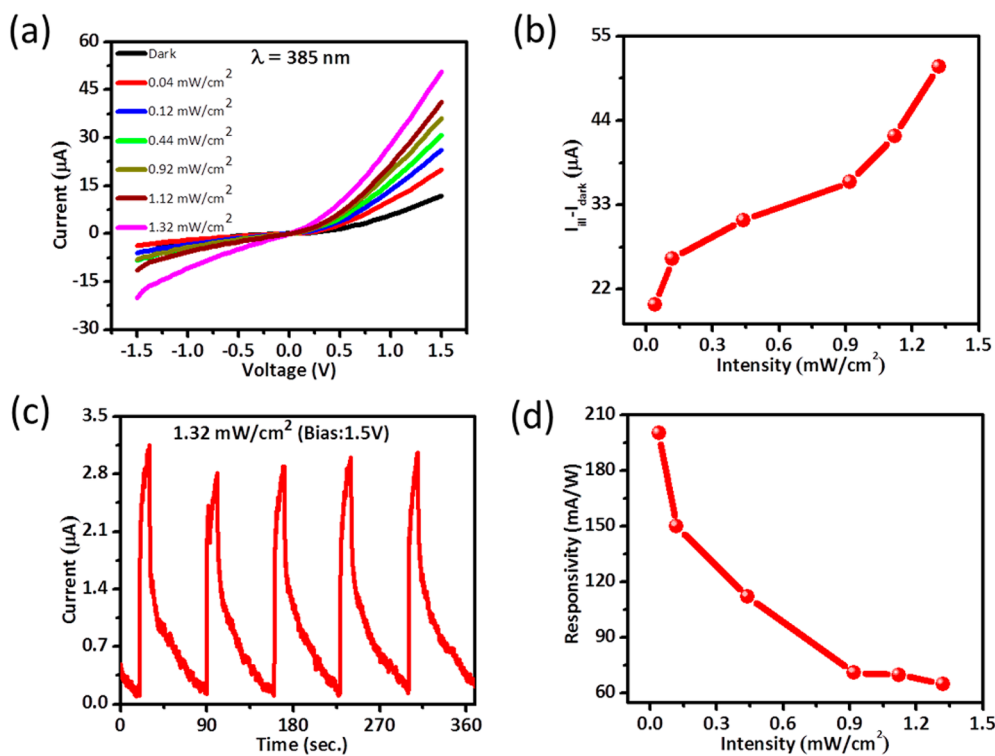


Figure 3. Electrical characterization of a ZnO/ZnS core/shell nanowire array device under UV illumination. (a) I – V measurements at different illumination densities, (b) illumination density dependence of photocurrent, (c) the device's on–off response, and (d) the variation in responsivity under several UV illumination densities.

The responsivity for UV (385 nm) excitation source, denoted as $R_{385\text{nm}}$, with a 0.04 mW/cm^2 illumination density, was found to be 0.2 A/W , which is similar to a single crystal ZnS nanobelt UV sensor²⁴ and is orders of magnitude higher than similar photodetectors fabricated with a 3D array of nanowires.^{25–30} This responsivity value corresponds to an external quantum efficiency (EQE) of about 65% if the internal photoconductive gain is assumed to be one.³¹ The high responsivity achieved in the ZnO/ZnS core/shell nanowire array device can mainly be attributed to the abrupt nature of the interface between ZnO and ZnS, which effectively inhibits carrier recombination and facilitates an efficient carrier separation.

The performance of the ZnO/ZnS core/shell nanowire array photodetector was also investigated under blue (465 nm) and green (520 nm) excitation source, and the results are summarized in Figures S2 and S3 (Supporting Information), respectively. It should be noted that the photon energy corresponding to blue (2.66 eV) and green (2.38 eV) wavelengths are significantly lower than those needed to promote direct band-to-band absorption in ZnO ($E_g \sim 3.2 \text{ eV}$)³² and ZnS ($E_g \sim 3.7 \text{ eV}$), which leads us to believe that the photocurrent response must be arising from an indirect type-II transition of electrons between the ZnS_{VBM} (shell) and ZnO_{CBM} (core). Remarkably, the photodetector response exhibits a similar behavior, as observed for UV (385 nm) excitation source (Figure 3). The peak photocurrents under blue and green excitations reached $\sim 44 \mu\text{A}$ (3 mW/cm^2 , Figure S2a (Supporting Information)) and $\sim 18 \mu\text{A}$ (3.2 mW/cm^2 , Figure S3a (Supporting Information)), respectively, which correspond to an increase of 267% for blue and 50% for green wavelength as compared to the $\sim 12 \mu\text{A}$ dark current. The photocurrent variation plot, with illumination intensities (Figures S2–S3b (Supporting Information)) and time dependence (Figures S2–S3c (Supporting Information)), shows electron–hole pair generation rate dependent linear increase of photocurrents in addition to fast and stable response as seen from the switching behavior of the device. It has been reported previously that strain at the heterostructure interface could reduce the natural band gap^{33–36} slightly, whereas only a staggered type-II band alignment could give rise to a much smaller band gap than either of the individual core or shell material.⁸

The strain and quantum confinement effect are the two reasons which may affect the natural type-II band gap ($\sim 1.93 \text{ eV}$) of ZnO/ZnS core/shell nanowire, and these two effects were considered to predict an effective energy gap at the ZnO/ZnS interface near 2 eV for very small core/shell nanowires.³⁷ In regard to the ZnO/ZnS core/shell nanowire diameter (150–200 nm), no quantum confinement effect can play a role in modifying the band gap although a weak effect of strain on type-II energy gap may exist. Figure 4 contains

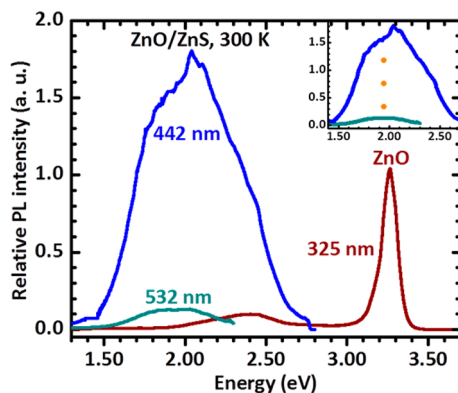


Figure 4. Room temperature PL for ZnO/ZnS core/shell nanowires collected with comparable laser power $\sim 145 \mu\text{W}$ under 532, 442, and 325 nm excitation, respectively. Spectra range from 1.3 eV to the edge of each laser's emission. ZnO produces green emission at 2.40 eV. Lower excitation energies produced broader type-II transition peaks. Inset: Magnification of the type-II transition PL peaks. The dotted orange line marks the broad peak center at $\sim 1.95 \text{ eV}$.

room temperature photoluminescence (PL) spectra measured with three excitation wavelengths: 325, 442, and 532 nm, where 325 nm excitation revealed ZnO band edge emission at 3.26 eV, but the ZnS band edge emission (3.7 eV) was not present, presumably due to the fact that ZnS shell is relatively thin.³⁸ Both blue (442 nm) and green (532 nm) lasers yield a broad band emission with its peak at around 2 eV, in general agreement with the predicted value for type-II transition.³⁶ Within this range, ZnO has defect-related peaks at 2.33 and 2.53 eV, respectively, while 2.64 eV (ZnS) and 2.25 eV (ZnO/ZnS) were previously reported with above bandgap excitation.^{39,40} These emissions are expected to be very weak under either 442 or 532 nm excitation. Both green emission quenching⁴¹ and weak ZnS emission³⁸ would result in some contributions that could lead to the broad emission band, which can be understood as resulting from structural fluctuations in nanowire core size and/or shell thickness and perhaps also some defect related transitions, as observed similarly in the type-II ZnO/ZnSe core/shell nanowire array.⁴² The dominant effect of the type-II transition⁴³ observed in photodetection measurements under blue and green excitation sources is mainly attributed to the abrupt interface between the ZnO core and ZnS shell.

Figures S2d–S3d (Supporting Information) contain responsivity vs intensity plots of the photodetector under blue and green illumination, respectively. Apparently, the responsivity values under blue and green excitation are smaller than under UV, mainly due to the absence of the direct band-to-band absorption in ZnO and weaker absorption at longer wavelengths.

To confirm that piezoelectric property of wurtzite, ZnO is unaffected by zinc blend ZnS shell layer deposition, a current versus time (I – T) measurement of the ZnO/ZnS core/shell nanowire array under cyclic strain

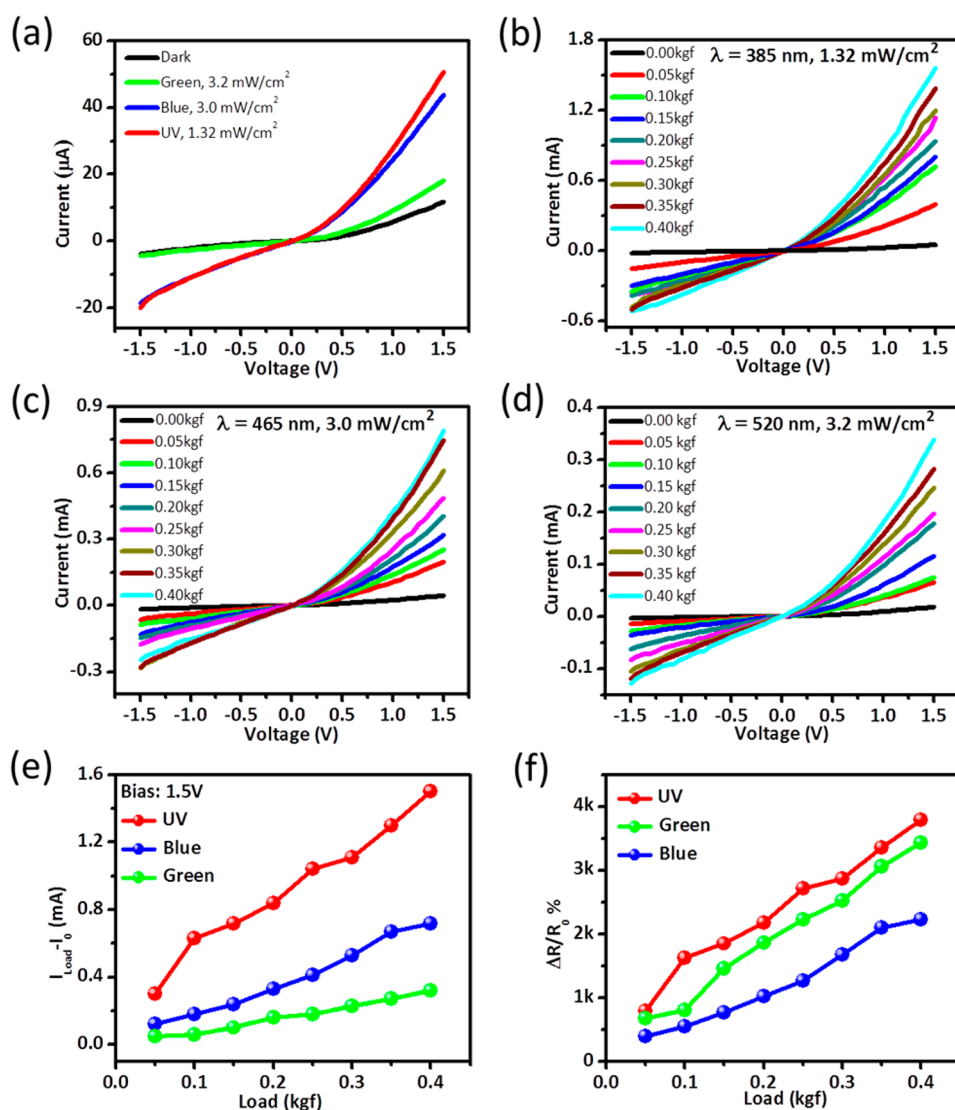


Figure 5. Electrical characterization of ZnO/ZnS core/shell nanowire array devices showing (a) the photocurrent response under dark, green, blue, and UV excitation, (b–d) photocurrent response at a fixed illumination densities of 1.32 mW/cm² (UV), 3.0 mW/cm² (blue) and 3.2 mW/cm² (green), respectively, with variable compressive loads. (e) Photocurrent response with respect to compressive loads and (f) the (%) change in responsivity with compressive loads.

both in dark and in the absence of any external bias was performed. Figure S1 (Supporting Information) represents the result of a typical I – T measurement where peak piezo-current exhibits an increase as the load increases, which is in accordance with earlier report.⁴⁴ Furthermore, to investigate the effect of the built-in piezopotential on photodetector performance, ZnO/ZnS core/shell nanowire array devices were subjected to compressive loads under UV, blue, and green excitation sources. Figure 5a is a typical I – V measurement of the device at peak illumination densities under UV, blue, and green excitation. In the absence of a compressive load, the peak photocurrent increases with the photon energy. Figure 5b displays the result of I – V measurements under a compressive load varying from 0.05 kg force (kgf) to 0.4 kgf at a UV illumination density of 1.32 mW/cm². It can be seen (Figure 5b) that increasing the compressive load results in an

increase in peak photocurrent under steady photon flux. Interestingly, the peak photocurrent (1.51 mA) at 0.4 kgf under steady state illumination is an order of magnitude (~ 31 times) higher than peak photocurrent without a load (51 μ A). A similar trend also appears in I – V measurements for blue (Figure 5c) and green (Figure 5d) excitation sources at fixed illumination intensities of 3 and 3.2 mW/cm², respectively, where the application of a compressive load resulted in a photocurrent change of an order of magnitude (~ 18 times) for blue and (~ 19 times) for green excitation sources compared to no load.

The change in peak photocurrent at compressive loads varying from 0.05 to 0.4 kgf for UV (1.32 mW/cm²), blue (3 mW/cm²), and green (3.2 mW/cm²) illumination at a bias of 1.5 V is summarized in Figure 5e, where the increasing photocurrent with compressive load is a trend. Additionally, the increment in peak photocurrent

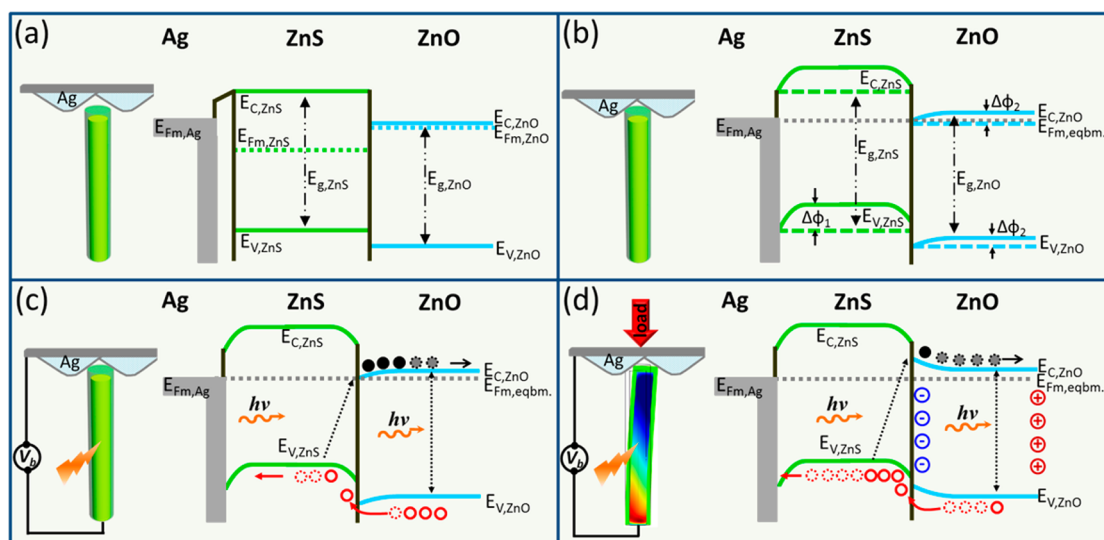


Figure 6. Equilibrium band position of an Ag/ZnS/ZnO interface (a) that demonstrates an abrupt, type-II band alignment at the ZnS/ZnO core/shell interface before the silver contact is made, (b) silver (Ag) contact with ZnS promotes Fermi level realignment that induces band bending (c) under illumination only, displaying direct band-to-band and an indirect type-II transition, and (d) under illumination with compressive strain together leading to a piezopotential-induced band bending. The core is wurtzite structured ZnO, and the shell is the zinc blend structured ZnS (in green color). Dotted line in (b) represents the initial position of the valence band maxima and the conduction band minima, whereas the solid lines represent the respective positions after band realignment and/or compression of a nanowire.

is found to be higher for UV illumination followed by blue and green illumination, which can be attributed to the combined effect of direct band-to-band UV absorption in ZnO and the type-II transition occurring from the ZnS_{VBM} to the ZnO_{CBM} . This band-to-band absorption for blue and green wavelengths, however, will not happen in either the ZnO core or the ZnS shell because of the very high/wide bandgap energies. This leads to photoabsorption only via an indirect type-II transition below individual core and shell bandgap energies.

Absolute responsivities calculated for a 0.4 kgf compressive load under UV (1.32 mW/cm^2), blue (3 mW/cm^2), and green (3.2 mW/cm^2) illumination at 1.5 V bias are 2.5, 0.54, and 0.13 A/W, respectively, which are at least an order of magnitude higher for all the illumination sources compared to no load conditions. A comparative change in responsivity, conventionally calculated as^{5,11} $(R_{\text{Load}} - R_0/R_0) \%$, where R_{Load} and R_0 are defined as responsivities with and without load, is displayed in Figure 5f. The (%) change in responsivity under compressive load observed in the ZnO/ZnS core/shell nanowire array photodetector is 3 orders of magnitude higher than the responsivity without a load.

The piezo-phototronic effect enhanced performance of ZnO/ZnS core/shell nanowire array photodetector under compressive load can be qualitatively explained through band diagram and realignment of band positions under the influence of the inner piezopotential. Figure 6 displays the relative band positions of a ZnO/ZnS core/shell nanowire in different configurations. As shown in Figure 6a, in the absence of silver (Ag) metal contact to ZnS, there is no net charge

transport across the junction because of staggered type-II band alignment where the Fermi level of ZnO is higher than that of ZnS, whereas the ZnS_{CBM} is higher than that for ZnO_{CBM} . Once silver contact to ZnS was made, the net electron transfer from silver to ZnS compensates the Fermi level imbalance, causing a downward bending of ZnS conduction and valence bands and also compensates ZnO Fermi level imbalance with minor downward band bending as shown in Figure 6b. Under UV illumination, as shown in Figure 6c, a direct band-to-band transition takes place only in ZnO, and a weak type-II transition occurs between the ZnS_{VBM} and ZnO_{CBM} . The type-II transition is a preferred absorption mode under both blue and green illumination. No significant Fermi level shift exists in ZnO and ZnS because of weak absorption under low illumination densities, whereas the net charge transfer between ZnO and ZnS is suppressed due to the barrier created for hole injection from ZnO to ZnS, and interface trap states for electron transport generated from downward bending of ZnO. The appearance of hole and electron trap state barriers ($\Delta\Phi_1$ and $\Delta\Phi_2$) are unfavorable for photosensing devices and can be tuned through the inner piezopotential to improve charge transport.

When nanowires are compressed under zigzag top electrode, each individual nanowire may undergo one of the three possible (Figure S4 (Supporting Information)) elastic deformation modes, resulting in a piezopotential distribution in ZnO core of ZnO/ZnS core/shell nanowire array. In view of slight off the vertical axis oriented growth of ZnO nanowires on ITO and high length/diameter (aspect) ratio (Figure 1a),

it is reasonable to believe that under externally applied load majority of the nanowires experienced shear deformation, as shown in Figure S4a (Supporting Information) for a single nanowire, that dominates the electrical transport properties of the device. However, the existence of either uniaxial compression (Figure S4b (Supporting Information)) or bending only (Figure S4c (Supporting Information)) mode of elastic deformation in few nanowires cannot be completely ruled out. In the absence of piezoelectric effect in zinc blend structured ZnS, the localized negative polarization charges appearing in ZnO⁴⁵ at the ZnO–ZnS interface bends the edges of valence (VB) and conduction bands (CB) of ZnO to higher energy (Figure 6d). It should be noted that in each outlined deformation mode (Figure S4a–c (Supporting Information)), the band position at ZnO–ZnS interface changes in similar manner provided we consider the negative polarization charges at the interface. This upward bending of bands of ZnO due to the presence of negative piezoelectric charges eliminates the pre-existing barrier $\Delta\Phi_2$ that is not favorable for the separation of electrons resulting in a quick separation of holes and electrons in ZnS and ZnO, respectively (Figure 6d), in addition to unaffected transport of type-II generated holes in ZnS. Both of these process acts synergistically to increase the conductance that results in higher current at the same bias and illumination compared to the no strain case. The moderate upward bending of ZnO valence and conduction band edges may not affect the type-II transition because the photon energies provided by blue and green excitation sources are still sufficiently high to promote electron transition from the ZnS_{VBM} to the ZnO_{CBM}

by eliminating the local trapping of electrons at the interface. Therefore, the electrons and holes are transported through the conductive channels provided by ZnO and ZnS, respectively. The piezoelectric polarization charges induced electron–hole separation is referred to as the piezo-phototronic effect,⁴⁶ and it explains the higher responsivity enhancement observed under blue and green illumination under compressive loads although the improvement is not as high as seen for UV illumination due to absence of direct band-to-band absorption.

CONCLUSIONS

In summary, an efficient and highly sensitive broadband UV/visible photodetector was successfully integrated on fully wide band gap ZnO/ZnS heterojunction 3D core/shell nanowire array. The abrupt interface between ZnO and ZnS plays a dominant role in photon absorption via an indirect type-II transition which was strongly manifested in the photodetection of visible illumination (blue and green). The absolute device responsivity was further increased through the piezo-phototronic effect by an order of magnitude under simultaneous application of load and illumination, resulting in three orders of change in the relative responsivity. This investigation demonstrates an efficient prototype UV/visible piezo-phototronic photodetector integrated on truly wide band gap 3D ZnO/ZnS core/shell nanowire array, in which the band gap limited photoabsorption is overcome by a type-II transition, which enables the use of wide band gap materials in broader (UV to visible) wavelength detection.

EXPERIMENTAL SECTION

ZnO nanowire array was synthesized on SiO₂ passivated indium tin oxide (ITO) coated glass substrate (CG801N, Delta Technologies LTD) by thermal evaporation of Zn powder in a two-zone furnace (GSL-1400X, MTL Corp). Briefly, 4 g of Zn powder (99.9%, metals basis, Alfa Aesar) was loaded in an alumina crucible and positioned at the center of the two-zone furnace. The SiO₂ passivated ITO/glass substrate was positioned at 25 cm downstream in the second zone of the furnace. The temperatures of the first and second zones were ramped to 900 and 550 °C under 350 standard cubic centimeter (sccm) Ar/O₂ (6:1) flow for the reaction time of 1 h. After reaction was complete, the furnace was cooled down to room temperature naturally and ZnO nanowires were formed in a white layer on ITO substrate.

To synthesize ZnO/ZnS core/shell nanowire array, the ITO substrate with ZnO nanowire array was transferred to a home-built pulsed laser deposition system (PLD) as described previously.⁹ Briefly, a ZnS target (99.99%, Kurt. J. Lesker) was loaded in the middle of the furnace and laser ablation was performed at 500 °C. ZnO nanowire on ITO substrate was positioned 3 cm away from the target, and ablation was performed for 20 min at 1 mTorr base pressure.

Structural and morphological characterizations were carried out with HITACHI Su8010 field-emission scanning electron microscope (FESEM) and a FEI Tecnai G2 F30 ST high-resolution transmission electron microscope (HRTEM) equipped with a

nanoprobe energy-dispersive (EDS) X-ray spectroscopy. Additional details of optical and structural characterizations can be found in a previously published literature.¹⁹ Room temperature photoluminescence (PL) measurements were measured by a Horiba LabRAM HR800 confocal Raman system with a Synapse charge-coupled detector (CCD). A 100× MPLAN objective lens (NA = 0.9) was used for 532 and 442 nm excitation, and a 50× UV objective lens (NA = 0.55) was used for 325 nm excitation. Laser powers were 148.2, 151.7, and 139.6 μW, respectively. Background measurements of the substrate were subtracted from all spectra.

As synthesized ZnO/ZnS core/shell nanowire array on ITO substrate was spin-coated by a thin layer of PMMA followed by O₂ plasma etching for a few minutes. For zigzag top electrode fabrication, polyester grating (12700 lines/inch, Edmund Optics) was sputter-coated with 30 nm of silver (Ag) and positioned on top of the nanowire array. ITO substrate and zigzag/Ag film were connected by copper leads using silver paste. A typical device photograph is shown in (Figure S5 (Supporting Information)) with total active device area of 30 mm². The electrical measurements were carried out using low noise current pre-amplifier (SR-570) and a source meter (Keithley 2401) coupled with a computer interface.

Conflict of Interest: The authors declare no competing financial interest.

Supporting Information Available: Performance of ZnO/ZnS core/shell nanowire as array as nanogenerator (1) and the same

device as a photodetector under (2) blue and (3) green illumination source, respectively. (4) Simulated cross-sectional piezopotential distribution under three different strain modes in an individual core/shell nanowire. (5) Photograph of a ZnO/ZnS core/shell nanowire array device. The Supporting Information is available free of charge on the ACS Publications website at DOI: 10.1021/acs.nano.5b02081.

Acknowledgment. This research at AMRI, UNO, was supported by the DARPA grant no. HR0011-07-1-0032 and research grants from Louisiana Board of Regents contract nos. LEQSF (2008-11)-RD-B-10 and LEQSF (2011-13)-RD-B-08. Y.Z. acknowledges the support of Bissell Distinguished Professorship at UNCC.

REFERENCES AND NOTES

- Wang, Z. L., *Piezotronics and Piezo-Phototronics*; Springer: New York, 2013.
- Feng, X.; Zhang, Y.; Wang, Z. Theoretical Study of Piezotronic Heterojunction. *Sci. China Technol. Sci.* **2013**, *56*, 2615–2621.
- Yang, Q.; Wang, W.; Xu, S.; Wang, Z. L. Enhancing Light Emission of ZnO Microwire-Based Diodes by Piezophototronic Effect. *Nano Lett.* **2011**, *11*, 4012–4017.
- Yang, Q.; Guo, X.; Wang, W.; Zhang, Y.; Xu, S.; Lien, D. H.; Wang, Z. L. Enhancing Sensitivity of a Single ZnO Micro-/Nanowire Photodetector by Piezo-phototronic Effect. *ACS Nano* **2010**, *4*, 6285–6291.
- Zhang, F.; Ding, Y.; Zhang, Y.; Zhang, X.; Wang, Z. L. Piezophototronic Effect Enhanced Visible and Ultraviolet Photodetection Using a ZnO–CdS Core/Shell Micro/nanowire. *ACS Nano* **2012**, *6*, 9229–9236.
- Boxberg, F.; Søndergaard, N.; Xu, H. Q. Photovoltaics with Piezoelectric Core/Shell Nanowires. *Nano Lett.* **2010**, *10*, 1108–1112.
- Pan, C.; Niu, S.; Ding, Y.; Dong, L.; Yu, R.; Liu, Y.; Zhu, G.; Wang, Z. L. Enhanced $\text{Cu}_2\text{S}/\text{CdS}$ Coaxial Nanowire Solar Cells by Piezo-phototronic Effect. *Nano Lett.* **2012**, *12*, 3302–3307.
- Zhang, Y.; Lin-Wang; Mascarenhas, A. Quantum Coaxial Cables for Solar Energy Harvesting. *Nano Lett.* **2007**, *7*, 1264–1269.
- Wang, K.; Chen, J.; Zhou, W.; Zhang, Y.; Yan, Y.; Pern, J.; Mascarenhas, A. Direct Growth of Highly Mismatched Type II ZnO/ZnSe Core/Shell Nanowire Arrays on Transparent Conducting Oxide Substrates for Solar Cell Applications. *Adv. Mater.* **2008**, *20*, 3248–3253.
- Wu, Z.; Zhang, Y.; Zheng, J.; Lin, X.; Chen, X.; Huang, B.; Wang, H.; Huang, K.; Li, S.; Kang, J. An All-Inorganic Type-II Heterojunction Array with Nearly Full Solar Spectral Response Based on ZnO/ZnSe Core/Shell Nanowires. *J. Mater. Chem.* **2011**, *21*, 6020–6026.
- Zhang, F.; Niu, S.; Guo, W.; Zhu, G.; Liu, Y.; Zhang, X.; Wang, Z. L. Piezo-phototronic Effect Enhanced Visible/UV Photodetector of a Carbon-Fiber/ZnO–CdS Double-Shell Microwire. *ACS Nano* **2013**, *7*, 4537–4544.
- Wang, Z.; Yu, R.; Pan, C.; Liu, Y.; Ding, Y.; Wang, Z. L. Piezo-Phototronic UV/Visible Photosensing with Optical-Fiber–Nanowire Hybridized Structures. *Adv. Mater.* **2015**, *10*, 1002/adma.201405274.
- Wallentin, J.; Anttu, N.; Asoli, D.; Huffman, M.; Åberg, I.; Magnusson, M. H.; Siefert, G.; Fuss-Kailuweit, P.; Dimroth, F.; Witzigmann, B.; Xu, H. Q.; Samuelson, L.; Deppert, K.; Borgström, M. T. InP Nanowire Array Solar Cells Achieving 13.8% Efficiency by Exceeding the Ray Optics Limit. *Science* **2013**, *339*, 1057–1060.
- Law, M.; Greene, L. E.; Johnson, J. C.; Saykally, R.; Yang, P. Nanowire Dye-Sensitized Solar Cells. *Nature Mater.* **2005**, *4*, 455–459.
- Yao, M.; Huang, N.; Cong, S.; Chi, C.-Y.; Seyed, M. A.; Lin, Y.-T.; Cao, Y.; Povinelli, M. L.; Dapkus, P. D.; Zhou, C. GaAs Nanowire Array Solar Cells with Axial p–i–n Junctions. *Nano Lett.* **2014**, *14*, 3293–3303.
- Liu, Y.; Yang, Q.; Zhang, Y.; Yang, Z.; Wang, Z. L. Nanowire Piezo-phototronic Photodetector: Theory and Experimental Design. *Adv. Mater.* **2012**, *24*, 1410–1417.
- Zhang, Y., ZnO and GaN Nanowire-Based Type II Heterostructures. In *Wide Band Gap Semiconductor Nanowires 2*; John Wiley & Sons, Inc.: New York, 2014; pp 85–103.
- Lu, M.-Y.; Song, J.; Lu, M.-P.; Lee, C.-Y.; Chen, L.-J.; Wang, Z. L. ZnO–ZnS Heterojunction and ZnS Nanowire Arrays for Electricity Generation. *ACS Nano* **2009**, *3*, 357–362.
- Wang, K.; Chen, J. J.; Zeng, Z. M.; Tarr, J.; Zhou, W. L.; Zhang, Y.; Yan, Y. F.; Jiang, C. S.; Pern, J.; Mascarenhas, A. Synthesis and Photovoltaic Effect of Vertically Aligned ZnO/ZnS Core/Shell Nanowire Arrays. *Appl. Phys. Lett.* **2010**, *96*, 123105.
- Wang, Y.; Zhan, X.; Wang, F.; Wang, Q.; Safdar, M.; He, J. Crystalline ZnO/ZnS_xSe_{1-x} Core/Shell Nanowire Arrays for Efficient Visible-Light Photoelectrocatalysis. *J. Mater. Chem., A* **2014**, *2*, 18413–18419.
- Wang, K.; Rai, S. C.; Marmon, J.; Chen, J.; Yao, K.; Wozny, S.; Cao, B.; Yan, Y.; Zhang, Y.; Zhou, W. Nearly Lattice Matched all Wurtzite CdSe/ZnTe Type-II Core/Shell Nanowires with Epitaxial Interfaces for Photovoltaics. *Nanoscale* **2014**, *6*, 3679–3685.
- Wang, X.; Song, J.; Liu, J.; Wang, Z. L. Direct-Current Nanogenerator Driven by Ultrasonic Waves. *Science* **2007**, *316*, 102–105.
- Soga, T., Preface. In *Nanostructured Materials for Solar Energy Conversion*; Soga, T., Ed.; Elsevier: Amsterdam, 2006; pp 3–43.
- Fang, X.; Bando, Y.; Liao, M.; Gautam, U. K.; Zhi, C.; Dierre, B.; Liu, B.; Zhai, T.; Sekiguchi, T.; Koide, Y.; Golberg, D. Single-Crystalline ZnS Nanobelts as Ultraviolet-Light Sensors. *Adv. Mater.* **2009**, *21*, 2034–2039.
- Vj, L.; Oh, J.; Nayak, A. P.; Katzenmeyer, A. M.; Gilchrist, K. H.; Grego, S.; Kobayashi, N. P.; Shih-Yuan, W.; Talin, A. A.; Dhar, N. K.; et al. A Perspective on Nanowire Photodetectors: Current Status, Future Challenges, and Opportunities. *IEEE J. Sel. Top. Quantum Electron.* **2011**, *17*, 1002–1032.
- Zhang, Z.; Liao, Q.; Yu, Y.; Wang, X.; Zhang, Y. Enhanced Photoresponse of ZnO Nanorods-Based Self-Powered Photodetector by Piezotronic Interface Engineering. *Nano Energy* **2014**, *9*, 237–244.
- Ni, P.-N.; Shan, C.-X.; Wang, S.-P.; Liu, X.-Y.; Shen, D.-Z. Self-Powered Spectrum-Selective Photodetectors Fabricated from n-ZnO/p-NiO Core/Shell Nanowire Arrays. *J. Mater. Chem., C* **2013**, *1*, 4445–4449.
- Zhu, H.; Shan, C. X.; Yao, B.; Li, B. H.; Zhang, J. Y.; Zhao, D. X.; Shen, D. Z.; Fan, X. W. High Spectrum Selectivity Ultraviolet Photodetector Fabricated from an n-ZnO/p-GaN Heterojunction. *J. Phys. Chem. C* **2008**, *112*, 20546–20548.
- Lin, P.; Chen, X.; Yan, X.; Zhang, Z.; Yuan, H.; Li, P.; Zhao, Y.; Zhang, Y. Enhanced Photoresponse of $\text{Cu}_2\text{O}/\text{ZnO}$ Heterojunction with Piezo-modulated Interface Engineering. *Nano Res.* **2014**, *7*, 860–868.
- Qin, L.; Shao, D.; Shing, C.; Sawyer, S. Wavelength Selective p-GaN/ZnO Colloidal Nanoparticle Heterojunction Photodiode. *Appl. Phys. Lett.* **2013**, *102*, 071106.
- Soci, C.; Zhang, A.; Xiang, B.; Dayeh, S. A.; Aplin, D. P. R.; Park, J.; Bao, X. Y.; Lo, Y. H.; Wang, D. ZnO Nanowire UV Photodetectors with High Internal Gain. *Nano Lett.* **2007**, *7*, 1003–1009.
- Srikant, V.; Clarke, D. R. On the Optical Band Gap of Zinc Oxide. *J. Appl. Phys.* **1998**, *83*, 5447–5451.
- Morke, M.; Weinhardt, L.; Lohmüller, B.; Heske, C.; Umbach, E.; Riedl, W.; Zweigart, S.; Karg, F. Flat Conduction-Band Alignment at the CdS/CuInSe₂ Thin-Film Solar-Cell Heterojunction. *Appl. Phys. Lett.* **2001**, *79*, 4482–4484.
- Moon, C.-Y.; Wei, S.-H.; Zhu, Y. Z.; Chen, G. D. Band-Gap Bowing Coefficients in Large Size-Mismatched II-VI Alloys: First-Principles Calculations. *Phys. Rev. B* **2006**, *74*, 233202.
- Haight, R.; Barkhouse, A.; Gunawan, O.; Shin, B.; Copel, M.; Hopstaken, M.; Mitzi, D. B. Band Alignment at the $\text{Cu}_2\text{ZnSn}(\text{S}_x\text{Se}_{1-x})_4/\text{CdS}$ Interface. *Appl. Phys. Lett.* **2011**, *98*, 253502.

36. Sun, L.; Haight, R.; Sinsermsuksakul, P.; Bok Kim, S.; Park, H. H.; Gordon, R. G. Band Alignment of SnS/Zn(O,S) Heterojunctions in SnS Thin-Film Solar-Cells. *Appl. Phys. Lett.* **2013**, *103*, 181904.
37. Schrier, J.; Demchenko, D. O.; Wang, Alivisatos, A. P. Optical Properties of ZnO/ZnS and ZnO/ZnTe Heterostructures for Photovoltaic Applications. *Nano Lett.* **2007**, *7*, 2377–2382.
38. Murphy, M. W.; Zhou, X. T.; Ko, J. Y. P.; Zhou, J. G.; Heigl, F.; Sham, T. K. Optical Emission of Biaxial ZnO–ZnS Nanoribbon Heterostructures. *J. Chem. Phys.* **2009**, *130*, 084707.
39. Wang, X.; Gao, P.; Li, J.; Summers, C. J.; Wang, Z. L. Rectangular Porous ZnO–ZnS Nanocables and ZnS Nanotubes. *Adv. Mater.* **2002**, *14*, 1732–1735.
40. Zhang, S.; Yin, B.; Jiang, H.; Qu, F.; Umar, A.; Wu, X. Hybrid ZnO/ZnS Nanoforests as the Electrode Materials for High Performance Supercapacitor Application. *Dalton Trans.* **2015**, *44*, 2409–2415.
41. Li, J.; Zhao, D.; Meng, X.; Zhang, Z.; Zhang, J.; Shen, D.; Lu, Y.; Fan, X. Enhanced Ultraviolet Emission from ZnS-Coated ZnO Nanowires Fabricated by Self-Assembling Method. *J. Phys. Chem. B* **2006**, *110*, 14685–14687.
42. Zhang, Y.; Wu, Z.; Zheng, J.; Lin, X.; Zhan, H.; Li, S.; Kang, J.; Bleuse, J.; Mariette, H. ZnO/ZnSe Type-II Core/Shell Nanowire Array Solar-Cell. *Sol. Energy Mater. Sol. Cells* **2012**, *102*, 15–18.
43. Vainorius, N.; Jacobsson, D.; Lehmann, S.; Gustafsson, A.; Dick, K. A.; Samuelson, L.; Pistol, M.-E. Observation of Type-II Recombination in Single Wurtzite/Zinc-Blende GaAs Heterojunction Nanowires. *Phys. Rev. B* **2014**, *89*, 165423.
44. Qin, Y.; Wang, X.; Wang, Z. L. Microfibre–Nanowire Hybrid Structure for Energy Scavenging. *Nature* **2008**, *451*, 809–813.
45. Gao, Y.; Wang, Z. L. Equilibrium Potential of Free Charge Carriers in a Bent Piezoelectric Semiconductive Nanowire. *Nano Lett.* **2009**, *9*, 1103–1110.
46. Han, C. B.; Zhang, C.; Tian, J.; Li, X.; Zhang, L.; Li, Z.; Wang, Z. L., Fundamental Theories of Piezotronics and Piezophotonics. *Nano Energy* **2014**, <http://dx.doi.org/10.1016/j.nanoen.2014.11.051>.